Journal of Computational Science 4 (2013) 12–23

Contents lists available at SciVerse ScienceDirect

Journal of Computational Science

journal homepage: www.elsevier.com/locate/jocs

Central schemes for the modified Buckley–Leverett equation

Ying Wang[a,b,*], Chiu-Yen Kao[a,c,1]

[a] Department of Mathematics, The Ohio State University, Columbus, OH 43210, United States
[b] School of Mathematics, University of Minnesota, Minneapolis, MN 55455, United States
[c] Department of Mathematics and Computer Science, Claremont Mckenna College, CA 91711, United States

ARTICLE INFO

Article history:
Received 21 October 2011
Received in revised form 19 January 2012
Accepted 6 February 2012
Available online 24 February 2012

MSC:
35L65
35L67
35K70
76S05
65M06
65M08

Keywords:
Conservation laws
Dynamic capillarity
Two-phase flows
Porous media
Shock waves
Pseudo-parabolic equations
Central schemes

ABSTRACT

In this paper, we extend the second and third order classical central schemes for the hyperbolic conservation laws to solve the modified Buckley–Leverett (MBL) equation which is of pseudo-parabolic type. The MBL equation describes two-phase flow in porous media, and it differs from the classical Buckley–Leverett (BL) equation by including a balanced diffusive–dispersive combination. The classical BL equation gives a monotone water saturation profile for any Riemann problem; on the contrast, when the dispersive parameter is large enough, the MBL equation delivers non-monotone water saturation profiles for certain Riemann problems as suggested by the experimental observations. Numerical results in this paper confirm the existence of non-monotone water saturation profiles consisting of constant states separated by shocks.

1. Introduction

The classical Buckley–Leverett (BL) equation [1] is a simple model for two-phase fluid flow in a porous medium. One application is secondary recovery by water-drive in oil reservoir simulation. In one space dimension the equation has the standard conservation form

$$\begin{aligned} u_t + (f(u))_x = 0 \quad &\text{in} \quad Q = \{(x,t) : x > 0, t > 0\} \\ u(x,0) = 0 \quad &\qquad x \in (0,\infty) \\ u(0,t) = u_B \quad &\qquad t \in [0,\infty) \end{aligned} \tag{1.1}$$

with the flux function $f(u)$ being defined as

$$f(u) = \begin{cases} 0 & u < 0, \\ \dfrac{u^2}{u^2 + M(1-u)^2} & 0 \le u \le 1, \\ 1 & u > 1. \end{cases} \tag{1.2}$$

In this content, $u : \overline{Q} \to [0,1]$ denotes the water saturation (e.g. $u = 1$ means pure water, and $u = 0$ means pure oil), u_B is a constant which indicates water saturation at $x = 0$, and $M > 0$ is the water/oil viscosity ratio. The classical BL Eq. (1.1) is a prototype for conservation laws with convex–concave flux functions. The graph of $f(u)$ and $f'(u)$ with $M = 2$ is given in Fig. 1.

The classical BL Eq. (1.1) has been well studied (see [10] for an introduction). Let α be the solution of $f'(u) = \frac{f(u)}{u}$, i.e.,

$$\alpha = \sqrt{\frac{M}{M+1}}. \tag{1.3}$$

The entropy solution of the classical BL equation can be classified into two categories:

* Corresponding author at: School of Mathematics, University of Minnesota, Minneapolis, MN 55455, United States.
E-mail addresses: wang@umn.edu (Y. Wang), kao@math.ohio-state.edu, ckao@cmc.edu (C.-Y. Kao).

[1] This work was supported in part by NSF Grant DMS-0811003 and an Alfred P. Sloan Fellowship.

1877-7503/$ – see front matter © 2012 Elsevier B.V. All rights reserved.
doi:10.1016/j.jocs.2012.02.001

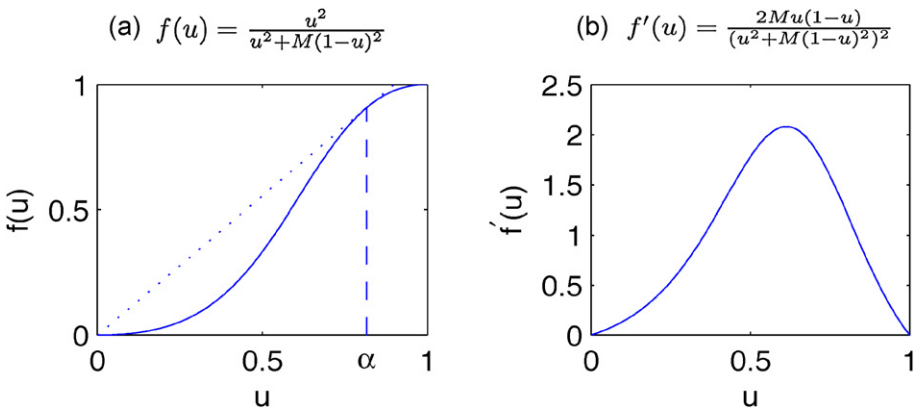

Fig. 1. $f(u)$ and $f'(u)$ with $M=2$.

1 If $0 < u_B \le \alpha$, the entropy solution has a single shock at $\frac{x}{t} = \frac{f(u_B)}{u_B}$.
2 If $\alpha < u_B < 1$, the entropy solution contains a rarefaction between u_B and α for $f'(u_B) < \frac{x}{t} < f'(\alpha)$ and a shock at $\frac{x}{t} = \frac{f(\alpha)}{\alpha}$.

These two types of solutions are shown in Fig. 2 for $M=2$. In either case, the entropy solution of the classical BL Eq. (1.1) is a non-increasing function of x at any given time $t>0$. However, the experiments of two-phase flow in porous medium reveal complex infiltration profiles, which may involve overshoot, i.e. profiles may not be monotone [4]. This suggests the need of modification to the classical BL Eq. (1.1).

Hassanizadeh and Gray [5,6] have included a third order mixed derivatives dispersive term, which models the *dynamic* effects in the capillary pressure difference between the two phases. Following the linearization and rescaling in [14–16], the modified Buckley–Leverett equation (MBL) is derived as

$$\frac{\partial u}{\partial t} + \frac{\partial f(u)}{\partial x} = \epsilon \frac{\partial^2 u}{\partial x^2} + \epsilon^2 \tau \frac{\partial^3 u}{\partial x^2 \partial t}, \tag{1.4}$$

where ϵ is the diffusion coefficient. van Duijn et al. [15] showed how ϵ and τ determine the type of the solution profile. In particular, for certain Riemann problems, the solution profile of (1.4) is not monotone when τ is larger than the threshold value τ_*, where τ_* was numerically determined to be 0.61 [15]. The non-monotonicity of the solution profile is consistent with the experimental observations [4].

The classical BL Eq. (1.1) is hyperbolic, and the numerical schemes for hyperbolic equations have been well developed (e.g. [10,11,2,3,13,8]). The MBL Eq. (1.4), however, is pseudo-parabolic. van Duijn et al. [15] have developed a first order finite difference scheme to solve the MBL Eq. (1.4). In this paper, we will illustrate how to extend the second and third order central schemes [13,8,9] to solve (1.4) numerically. The local discontinuous Galerkin method has been applied to solve equations involving mixed derivatives u_{xxt} term [18,19]. To the best knowledge of the authors, the central schemes have not been applied to solve equations of this kind. The main advantage of the central schemes is the simplicity. The "direction of the wind" is not required to be identified, and hence the field-by-field decomposition can be avoided.

Unlike the finite domain of dependence for the classical BL Eq. (1.1), the domain of dependence for the MBL Eq. (1.4) is infinite. This naturally raises the question for the choice of computational domain. To answer this question, Wang et al. [17] studied the MBL equation equipped with two types of domains, one is the half line domain $x \in [0, +\infty)$, and the other one is finite interval domain $x \in [0, L]$. Wang et al. [17] have shown that the difference between the solutions of these two types of problems decays exponentially with respect to the length of the interval L for practically interesting initial profiles. This provides a theoretical justification for the choice of the computational domain. Therefore, the numerical results in this paper are sought on the finite interval domain $x \in [0, L]$ with sufficiently large L.

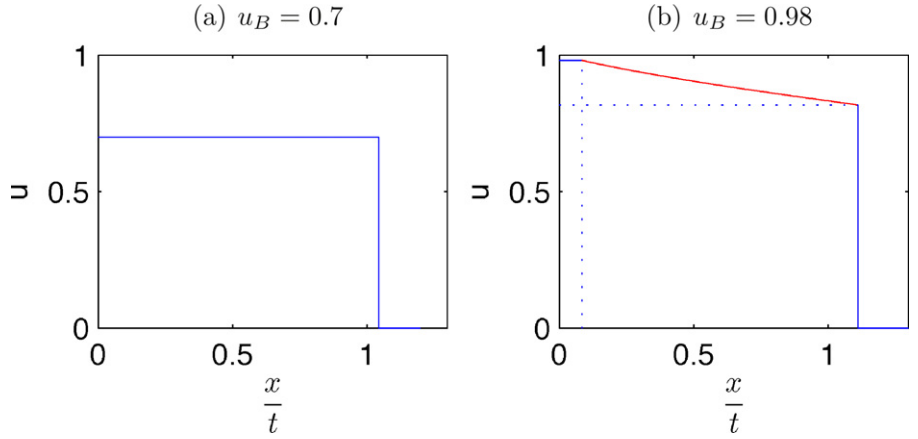

Fig. 2. The entropy solution of the classical BL equation ($M=2, \alpha = \sqrt{\frac{2}{3}} \approx 0.8165$). (a) $0 < u_B = 0.7 \le \alpha$, the solution consists of one shock at $\frac{x}{t} = \frac{f(u_B)}{u_B}$; (b) $\alpha < u_B = 0.98 < 1$, the solution consists of a rarefaction between u_B and α for $f'(u_B) < \frac{x}{t} < f'(\alpha)$ and a shock at $\frac{x}{t} = \frac{f(\alpha)}{\alpha}$.

The organization of this paper is as follows. In Section 2, the second and third order central schemes will be developed for MBL equation in the finite interval domain. We provide a detailed derivation on how to extend the central schemes [13,8] for conservation laws to solve the MBL Eq. (1.4). The idea of adopting numerical schemes originally designed for hyperbolic equations to pseudo-parabolic equations is not restricted to central type schemes only [18,19]. The numerical results in Section 3 show that the water saturation profile strongly depends on the dispersive parameter τ value as studied in [15]. For $\tau > \tau_*$, the MBL Eq. (1.4) gives non-monotone water saturation profiles for certain Riemann problems as suggested by experimental observations [4]. Section 4 gives the conclusion of the paper and the possible future directions.

2. Numerical schemes

In this section, we show how to apply the central schemes [13,8] originally designed for hyperbolic conservation laws to numerically solve the MBL Eq. (1.4), which is of pseudo-parabolic type. Specifically, we solve the following finite domain initial boundary value problem

$$\begin{aligned} &u_t + (f(u))_x = \epsilon u_{xx} + \epsilon^2 \tau u_{xxt} \qquad x \in (0, L),\ t > 0 \\ &u(x, 0) = u_B \chi_{\{x=0\}} + 0\chi_{\{0<x\le L\}} \\ &u(0, t) = u_B, \quad u(L, t) = 0. \end{aligned} \tag{2.1}$$

We first collect all the terms with time derivative and rewrite MBL Eq. (1.4) as

$$(u - \epsilon^2 \tau u_{xx})_t + (f(u))_x = \epsilon u_{xx}. \tag{2.2}$$

By letting

$$w = u - \epsilon^2 \tau u_{xx} \quad \Leftrightarrow \quad u = (I - \epsilon^2 \tau \partial_{xx})^{-1} w, \tag{2.3}$$

MBL Eq. (2.2) can be written as

$$w_t + (f(u))_x = \epsilon u_{xx}. \tag{2.4}$$

Now, the new form of MBL Eq. (2.4) can be viewed as a PDE in terms of w, and the occurrence of u can be recovered by (2.3). Eq. (2.4) can be formally viewed as

$$w_t + (f((I - \epsilon^2 \tau \partial_{xx})^{-1} w))_x = \epsilon((I - \epsilon^2 \tau \partial_{xx})^{-1} w)_{xx}, \tag{2.5}$$

which is a balance law in term of w. In this section, we demonstrate how to apply the second and third order central schemes to solve the MBL Eq. (2.2).

2.1. Second-order schemes

In this section, we show how to apply the classical second order central schemes [13] originally designed for hyperbolic conservation laws to numerically solve the MBL Eq. (1.4), which is of pseudo-parabolic type. To solve (2.4), we modify the central scheme given in [13]. As in [13], at each time level, we first reconstruct a piecewise linear approximation of the form

$$L_j(x, t) = w_j(t) + (x - x_j)\frac{w_j'}{\Delta x}, \qquad x_{j-\frac{1}{2}} \le x \le x_{j+\frac{1}{2}}. \tag{2.6}$$

Second-order accuracy is guaranteed if the so-called vector of numerical derivative $\frac{w_j'}{\Delta x}$, which will be given later, satisfies

$$\frac{w_j'}{\Delta x} = \frac{\partial w(x_j, t)}{\partial x} + \mathcal{O}(\Delta x). \tag{2.7}$$

We denote the staggered piecewise-constant functions $\overline{w}_{j+\frac{1}{2}}(t)$ as

$$\overline{w}_{j+\frac{1}{2}}(t) = \frac{1}{\Delta x}\int_{x_j}^{x_{j+1}} w(x, t)\, dx. \tag{2.8}$$

Evolve the piecewise linear interplant (2.6) by integrating (2.4) over $[x_j, x_{j+1}] \times [t, t + \Delta t]$

$$\begin{aligned} &\overline{w}_{j+\frac{1}{2}}(t + \Delta t) \\ &= \overline{w}_{j+\frac{1}{2}}(t) - \frac{1}{\Delta x}\left[\int_t^{t+\Delta t} f(u(x_{j+1}, s))\, ds - \int_t^{t+\Delta t} f(u(x_j, s))\, ds\right] \\ &\quad + \frac{\epsilon}{\Delta x}\left[\int_t^{t+\Delta t}\int_{x_j}^{x_{j+1}} \frac{\partial^2 u(x, s)}{\partial x^2}\, dx\, ds\right]. \end{aligned} \tag{2.9}$$

We calculate each term on the right hand side of (2.9) below. For $\overline{w}_{j+\frac{1}{2}}(t)$, applying the definition of $L_j(x, t)$ and $L_{j+1}(x, t)$ given in (2.6) to (2.8), we have that

$$\begin{aligned} \overline{w}_{j+\frac{1}{2}}(t) &= \frac{1}{\Delta x}\int_{x_j}^{x_{j+\frac{1}{2}}} L_j(x, t)\, dx + \frac{1}{\Delta x}\int_{x_{j+\frac{1}{2}}}^{x_{j+1}} L_{j+1}(x, t)\, dx \\ &= \frac{1}{2}(w_j(t) + w_{j+1}(t)) + \frac{1}{8}(w_j' - w_{j+1}'). \end{aligned} \tag{2.10}$$

The middle two integrands can be approximated by the midpoint rule

$$\begin{aligned} \int_t^{t+\Delta t} f\left(u\left(x_j, s\right)\right)\, ds &= f\left(u\left(x_j, t + \frac{\Delta t}{2}\right)\right)\Delta t + \mathcal{O}\left(\Delta t^3\right) \\ \int_t^{t+\Delta t} f\left(u\left(x_{j+1}, s\right)\right)\, ds &= f\left(u\left(x_{j+1}, t + \frac{\Delta t}{2}\right)\right)\Delta t + \mathcal{O}\left(\Delta t^3\right) \end{aligned} \tag{2.11}$$

if the CFL condition

$$\lambda \cdot \max_{x_j \le x \le x_{j+1}} \left|\frac{\partial f(u(w(x, t)))}{\partial w}\right| < \frac{1}{2}, \qquad \text{where} \quad \lambda = \frac{\Delta t}{\Delta x}$$

is met. For MBL Eq. (2.4), we have that at $t > 0$,

$$u - \epsilon^2 \tau u_{xx} = w, \qquad u(0) = w(0), \qquad u(L) = w(L). \tag{2.12}$$

To solve the boundary value problem (2.12), we let $v(x) = \frac{(L-x)w(0) + xw(L)}{L}$, then

$$u(x) = [(I - \epsilon^2 \tau \partial_{xx})^{-1} w](x) = v(x) + \frac{1}{L}\int_0^L [w(y) - v(y)]\, K(x, y)\, dy$$

where

$$K(x, y) = \sum_{k=1}^{\infty} \frac{\sin\left(\frac{k\pi x}{L}\right)\sin\left(\frac{k\pi y}{L}\right)}{1 + \left(\frac{k\pi}{L}\right)^2 \epsilon^2 \tau}.$$

Hence the eigenvalues for $(I - \epsilon^2 \tau \partial_{xx})^{-1}$ are

$$\lambda_k = \frac{1}{1 + \left(\frac{k\pi}{L}\right)^2 \epsilon^2 \tau} \le 1, \qquad k = 1, 2, 3 \ldots$$

Therefore, the CFL condition is

$$\begin{aligned} &\frac{\Delta t}{\Delta x} \cdot \max_{x_j \le x \le x_{j+1}} \left|\frac{\partial f(u(w(x, t)))}{\partial w}\right| \\ &= \frac{\Delta t}{\Delta x} \cdot \max_{\substack{x_j \le x \le x_{j+1} \\ k = 1, 2, 3 \ldots}} \left|\frac{\partial f(u(x, t))}{\partial u}\right| \cdot \lambda_k \\ &\le \frac{\Delta t}{\Delta x} \cdot 2.2 < \frac{1}{2} \end{aligned}$$

In the numerical computations in Section 3, we chose $\frac{\Delta t}{\Delta x} = 0.1$. In (2.11), to estimate $u\left(\cdot, t+\frac{\Delta t}{2}\right)$'s, we use Taylor expansion and the conservation law (2.4):

$$\begin{aligned} w(x_j, t+\frac{\Delta t}{2}) &= w_j(t) + \frac{\partial w}{\partial t}\frac{\Delta t}{2} + \mathcal{O}(\Delta t^2) \\ &= w_j(t) + \left(\epsilon\frac{\partial^2 u}{\partial x^2} - \frac{\partial f}{\partial x}\right)\frac{\Delta t}{2} + \mathcal{O}(\Delta t^2) \\ &= w_j(t) + (\epsilon \Delta x D^2 u_j - f_j')\frac{\lambda}{2}, \end{aligned} \tag{2.13}$$

where D is the discrete central difference operator

$$D^2 u_j = \frac{u_{j-1} - 2u_j + u_{j+1}}{\Delta x^2},$$

and the second-order accuracy is met if

$$\frac{f_j'}{\Delta x} = \frac{\partial f(u(x_j, t))}{\partial x} + \mathcal{O}(\Delta x). \tag{2.14}$$

The choices for $\{w_j'\}$ in (2.7) and $\{f_j'\}$ in (2.14) can be found in [13], and we chose

$$w_j' = MM\{\Delta w_{j+\frac{1}{2}}, \Delta w_{j-\frac{1}{2}}\}\ , \qquad f_j' = MM\{\Delta f_{j+\frac{1}{2}}, \Delta f_{j-\frac{1}{2}}\} \tag{2.15}$$

where $MM\{x, y\} = \text{minmod}(x, y) = \frac{1}{2}(\text{sgn}(x) + \text{sgn}(y)) \cdot \text{Min}(|x|, |y|)$ and $\Delta w_{j+\frac{1}{2}} = w_{j+1} - w_j$. Notice that (2.15) determines w_j' and f_j' values ultimately based on one-sided difference, which makes the proposed schemes not purely central. However, this choice ensures the proposed schemes to be non-oscillatory.

Combining (2.9)–(2.11), we obtain

$$\begin{aligned} \overline{w}_{j+\frac{1}{2}}(t+\Delta t) = \ & \overline{w}_{j+\frac{1}{2}}(t) \\ & -\lambda\left[f\left(u_{j+1}\left(t+\frac{\Delta t}{2}\right)\right) - f\left(u_j\left(t+\frac{\Delta t}{2}\right)\right)\right] \\ & +\frac{\epsilon}{\Delta x}\left[\int_t^{t+\Delta t}\int_{x_j}^{x_{j+1}} \frac{\partial^2 u(x,s)}{\partial x^2}\, dx\, ds\right]. \end{aligned} \tag{2.16}$$

Next, we will re-write (2.16) in terms of u. $(\overline{u_{xx}})_{j+\frac{1}{2}}$ is approximated as

$$(\overline{u_{xx}})_{j+\frac{1}{2}} = \frac{1}{\Delta x}\int_{x_j}^{x_{j+1}} u_{xx}\, dx = \frac{1}{\Delta x}(u_x(x_{j+1}, t) - u_x(x_j, t)),$$

and using the cell averages, it becomes

$$\begin{aligned} (\overline{u_{xx}})_{j+\frac{1}{2}} &= \frac{1}{\Delta x}\left(\frac{\overline{u}_{j+3/2} - \overline{u}_{j+1/2}}{\Delta x} - \frac{\overline{u}_{j+1/2} - \overline{u}_{j-1/2}}{\Delta x}\right) \\ &= \frac{\overline{u}_{j+3/2} - 2\overline{u}_{j+1/2} + \overline{u}_{j-1/2}}{(\Delta x)^2} \\ &= D^2\overline{u}_{j+\frac{1}{2}}. \end{aligned} \tag{2.17}$$

Notice that the linear interpolation (similar to (2.6))

$$\tilde{L}_{j+\frac{1}{2}}(x, t+\Delta t) = u_{j+\frac{1}{2}}(t+\Delta t) + (x - x_{j+\frac{1}{2}})\frac{u'_{j+\frac{1}{2}}}{\Delta x}$$

for $x_j \le x \le x_{j+1}$

and the cell average definition (similar to (2.8))

$$\overline{u}_{j+\frac{1}{2}}(t+\Delta t) = \frac{1}{\Delta t}\int_{x_j}^{x_{j+1}} u(x, t+\Delta t)\, dx$$

ensure that

$$\overline{u}_{j+\frac{1}{2}}(t+\Delta t) = u_{j+\frac{1}{2}}(t+\Delta t),$$

and the convertion between u and w is done using the following relation

$$(I - \epsilon^2\tau D^2)u = w. \tag{2.18}$$

Hence re-writting (2.16) in terms of u gives the staggered central scheme

$$\begin{aligned} & (I - \epsilon^2\tau D^2)u_{j+\frac{1}{2}}(t+\Delta t) \\ & = (I - \epsilon^2\tau D^2)\overline{u}_{j+\frac{1}{2}}(t) \\ & \quad -\lambda\left[f\left(u_{j+1}\left(t+\frac{\Delta t}{2}\right)\right) - f\left(u_j\left(t+\frac{\Delta t}{2}\right)\right)\right] \\ & \quad +\frac{\epsilon}{\Delta x}\left[\int_t^{t+\Delta t}\int_{x_j}^{x_{j+1}} \frac{\partial^2 u(x,s)}{\partial x^2}\, dx\, ds\right]. \end{aligned} \tag{2.19}$$

We will focus on the last integral in (2.19). There are many ways to numerically calculate this integral. We will show two ways to do this in the following two subsections, both of them achieve second order accuracy.

2.1.1. Trapezoid scheme

In this scheme, we use the notion (2.8) and the trapezoid rule to calculate the integral numerically as follows:

$$\begin{aligned} & \int_t^{t+\Delta t}\int_{x_j}^{x_{j+1}} \frac{\partial^2 u(x,s)}{\partial x^2}\, dx\, ds \\ & = \Delta x\int_t^{t+\Delta t} (\overline{u_{xx}})_{j+\frac{1}{2}}(s)\, ds \\ & = \frac{\Delta x \Delta t}{2}\left((\overline{u_{xx}})_{j+\frac{1}{2}}(t) + (\overline{u_{xx}})_{j+\frac{1}{2}}(t+\Delta t)\right) \end{aligned} \tag{2.20}$$

with $\mathcal{O}(\Delta t^3)$ error. Combining with (2.17) and (2.19), we can get the trapezoid scheme

$$\begin{aligned} & \left(I - \left(\epsilon^2\tau + \frac{\epsilon\Delta t}{2}\right)D^2\right)u_{j+\frac{1}{2}}(t+\Delta t) \\ & = \left(I - \left(\epsilon^2\tau - \frac{\epsilon\Delta t}{2}\right)D^2\right)\overline{u}_{j+\frac{1}{2}}(t) \\ & \quad -\lambda\left[f\left(u_{j+1}\left(t+\frac{\Delta t}{2}\right)\right) - f\left(u_j\left(t+\frac{\Delta t}{2}\right)\right)\right]. \end{aligned} \tag{2.21}$$

The flow chart of the trapezoid scheme is given in (2.22)

$$\begin{array}{ccccccc} & & \overline{w}_{j+\frac{1}{2}}(t) & \xrightarrow{(2.18)} & \overline{u}_{j+\frac{1}{2}}(t) & & \\ & \overset{(2.10)}{\nearrow} & & & & \overset{(2.21)}{\searrow} & \\ u_j(t) \xrightarrow{(2.18)} w_j(t) & & & & & & u_{j+\frac{1}{2}}(t+\Delta t) \\ & \underset{(2.13)}{\searrow} & & & & \underset{(2.21)}{\nearrow} & \\ & & w_j(t+\frac{\Delta t}{2}) & \xrightarrow{(2.18)} & u_j(t+\frac{\Delta t}{2}) & & \end{array} \tag{2.22}$$

2.1.2. Midpoint scheme

In this scheme, we use the notion (2.8) and the midpoint rule to calculate the integral numerically as follows:

$$\int_t^{t+\Delta t}\int_{x_j}^{x_{j+1}} \frac{\partial^2 u(x,s)}{\partial x^2}\,dx\,ds = \Delta x \int_t^{t+\Delta t} (\overline{u_{xx}})_{j+\frac{1}{2}}(s)\,ds$$
$$= \Delta x \Delta t (\overline{u_{xx}})_{j+\frac{1}{2}}(t+\frac{\Delta t}{2}).$$

Combining with (2.17) and (2.19), we can get the midpoint scheme

$$\begin{aligned}&(I-\epsilon^2\tau D^2)u_{j+\frac{1}{2}}(t+\Delta t)\\ &= \overline{w}_{j+\frac{1}{2}}(t) - \lambda\left[f\left(u_{j+1}\left(t+\frac{\Delta t}{2}\right)\right) - f\left(u_j\left(t+\frac{\Delta t}{2}\right)\right)\right]\\ &\quad + \epsilon\Delta t D^2 \overline{u}_{j+\frac{1}{2}}(t+\frac{\Delta t}{2}).\end{aligned} \tag{2.23}$$

The flow chart of the midpoint scheme is given in (2.24)

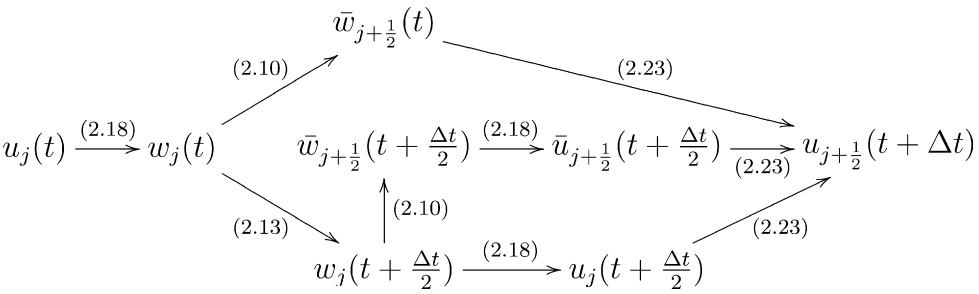

(2.24)

2.2. A third order semi-discrete scheme

Similarly, we can extend the third order scheme to solve MBL Eq. (1.4), however, it is more involved. But the third order semi-discrete central scheme proposed in [8] can be extended to solve the MBL equation in a straightforward manner. In order to make the paper self-contained, we include the formulation below.

$$\frac{d\overline{w}_j}{dt} = -\frac{H_{j+1/2}(t) - H_{j-1/2}(t)}{\Delta x} + \epsilon Q_j(t)$$

where $\overline{w}(x,t)$ denotes the cell average of w

$$\overline{w}_j(t) = \frac{1}{\Delta x}\int_{x_{j-1/2}}^{x_{j+1/2}} w(x,t)\,dx,$$

$H_{j+1/2}(t)$ is the numerical convection flux and $Q_j(t)$ is a high-order approximation to the diffusion term u_{xx}

$$H_{j+1/2}(t) = \frac{f(u^+_{j+1/2}(t)) + f(u^-_{j+1/2}(t))}{2} - \frac{a_{j+1/2}(t)}{2}\left[w^+_{j+1/2}(t) - w^-_{j+1/2}(t)\right]$$

where $u^-_{j+1/2}(t), u^+_{j+1/2}(t)$ denote the left and right intermediate values of $u(x,t^n)$ at $x_{j+1/2}$, and their values are converted from the $w^-_{j+1/2}(t), w^+_{j+1/2}(t)$ using (2.3). The way to calculate$w^-_{j+1/2}(t)$, $w^+_{j+1/2}(t)$ and $a_{j+1/2}(t)$ is

$$\begin{aligned} w^+_{j+1/2}(t) &= A_{j+1} - \frac{\Delta x}{2}B_{j+1} + \frac{(\Delta x)^2}{8}C_{j+1},\\ w^-_{j+1/2}(t) &= A_j + \frac{\Delta x}{2}B_j + \frac{(\Delta x)^2}{8}C_j,\\ a_{j+1/2}(t) &= \max\left\{\frac{\partial f}{\partial u}(u^-_{j+1/2}(t)), \frac{\partial f}{\partial u}(u^+_{j+1/2}(t))\right\},\end{aligned}$$

where

$$\begin{aligned} A_j &= \overline{w}^n_j - \frac{G^j_C}{12}(\overline{w}^n_{j+1} - 2\overline{w}^n_j + \overline{w}^n_{j-1}),\\ B_j &= \frac{1}{\Delta x}\left[G^j_R(\overline{w}^n_{j+1} - \overline{w}^n_j) + G^j_C\frac{\overline{w}^n_{j+1} - \overline{w}^n_{j-1}}{2} + G^j_L(\overline{w}^n_j - \overline{w}^n_{j-1})\right],\\ C_j &= 2G^j_C\frac{\overline{w}^n_{j-1} - 2\overline{w}^n_j + \overline{w}^n_{j+1}}{\Delta x^2},\\ G^j_i &= \frac{\alpha^j_i}{\sum_m \alpha^j_m} \qquad \alpha^j_i = \frac{c_i}{(\epsilon_0 + IS^j_i)^p}, \qquad i,m \in \{C,R,L\}\\ c_L &= c_R = 1/4, \qquad c_C = 1/2, \qquad \epsilon_0 = 10^{-6}, \qquad p = 2,\\ IS^j_L &= (\overline{w}^n_j - \overline{w}^n_{j-1})^2, \qquad IS^j_R = (\overline{w}^n_{j+1} - \overline{w}^n_j)^2,\\ IS^j_C &= \frac{13}{3}(\overline{w}^n_{j+1} - 2\overline{w}^n_j + \overline{w}^n_{j-1})^2 + \frac{1}{4}(\overline{w}^n_{j+1} - \overline{w}^n_{j-1})^2.\end{aligned}$$

The diffusion u_{xx} is approximated using the following fourth-order central differencing form

$$Q_j(t) = \frac{-\overline{u}_{j-2} + 16\overline{u}_{j-1} - 30\overline{u}_j + 16\overline{u}_{j+1} - \overline{u}_{j+2}}{12\Delta x^2}. \tag{2.25}$$

The boundary conditions (2.1) are extended to the ghost points at the boundaries. The scheme is semi-discrete in the sense that the discretization is done in space first, and then the time evolution equation can be solved as a system of ordinary differential equations using any ODE solver of third order or higher. In this paper, we simply use the standard fourth order Runge–Kutta methods. Notice that to achieve the third order accuracy, the linear solver that converts u from w using (2.3) need also to be high order, and (2.25) is used to discretize u_{xx} in our convertion.

3. Computational results

In this section, we show the numerical solutions to the MBL equation

$$\begin{aligned} &u_t + (f(u))_x = \epsilon u_{xx} + \epsilon^2\tau u_{xxt} \qquad x\in(0,L),\ t>0\\ &u(x,0) = u_B\chi_{\{x=0\}} + 0\chi_{\{0<x\le L\}}\\ &u(0,t) = u_B, \quad u(L,t) = 0.\end{aligned} \tag{3.1}$$

To validate the order analysis given in Section 2 for various schemes proposed, we first test the order of our schemes numerically with a smooth initial condition

$$u_0(x) = u_B H(x-5,5),$$

where

$$H(x,\xi) = \begin{cases} 1 & \text{if } x < -\xi\\ 1 - \frac{1}{2}\left(1 + \frac{x}{\xi} + \frac{1}{\pi}\sin\left(\frac{\pi x}{\xi}\right)\right) & \text{if } -\xi \le x \le \xi\\ 0 & \text{if } x > \xi\end{cases}.$$

Table 1
The accuracy test for the trapezoid scheme for the MBL Eq. (3.1) with $\epsilon = 1$ and $M = 2$.

	N	$\left\|\left\| u_{\Delta x} - u_{\frac{\Delta x}{2}} \right\|\right\|_1$	Order	$\left\|\left\| u_{\Delta x} - u_{\frac{\Delta x}{2}} \right\|\right\|_2$	Order	$\left\|\left\| u_{\Delta x} - u_{\frac{\Delta x}{2}} \right\|\right\|_\infty$	Order
	60	7.5416e−03	–	2.5388e−03	–	1.5960e−03	–
$u_B = 0.9$	120	1.9684e−03	1.9379	6.7288e−04	1.9157	4.4066e−04	1.8568
$\tau = 0.2$	240	4.9891e−04	1.9802	1.7645e−04	1.9311	1.2529e−04	1.8144
	480	1.2589e−04	1.9865	4.5366e−05	1.9596	3.3205e−05	1.9158
	60	8.0141e−03	–	2.6069e−03	–	1.4989e−03	–
$u_B = 0.9$	120	2.1502e−03	1.8981	7.0452e−04	1.8876	4.2221e−04	1.8279
$\tau = 1$	240	5.5697e−04	1.9488	1.8259e−04	1.9480	1.1283e−04	1.9038
	480	1.4104e−04	1.9815	4.6109e−05	1.9855	2.8719e−05	1.9740
	60	1.3102e−02	–	4.1784e−03	–	2.2411e−03	–
$u_B = 0.9$	120	3.6201e−03	1.8557	1.0994e−03	1.9263	6.1060e−04	1.8759
$\tau = 5$	240	9.6737e−04	1.9039	2.8089e−04	1.9686	1.5667e−04	1.9625
	480	2.5825e−04	1.9053	7.1250e−05	1.9790	3.9286e−05	1.9956
	60	6.4427e−03	–	2.1578e−03	–	1.1682e−03	–
$u_B = \alpha$	120	1.6611e−03	1.9555	5.7775e−04	1.9011	3.6447e−04	1.6804
$\tau = 0.2$	240	4.3643e−04	1.9283	1.5215e−04	1.9250	1.0389e−04	1.8107
	480	1.1223e−04	1.9593	3.9170e−05	1.9577	2.7629e−05	1.9109
	60	7.5867e−03	–	2.4101e−03	–	1.3364e−03	–
$u_B = \alpha$	120	2.0069e−03	1.9185	6.4998e−04	1.8906	3.7650e−04	1.8277
$\tau = 1$	240	5.1832e−04	1.9531	1.6801e−04	1.9519	1.0062e−04	1.9037
	480	1.3136e−04	1.9803	4.2497e−05	1.9831	2.5599e−05	1.9748
	60	1.1959e−02	–	3.8026e−03	–	1.9938e−03	–
$u_B = \alpha$	120	3.2940e−03	1.8602	9.9527e−04	1.9338	5.4231e−04	1.8783
$\tau = 5$	240	8.7736e−04	1.9086	2.5358e−04	1.9727	1.3933e−04	1.9606
	480	2.3271e−04	1.9146	6.4252e−05	1.9806	3.4967e−05	1.9944
	60	5.7714e−03	–	1.9358e−03	–	1.0481e−03	–
$u_B = 0.75$	120	1.5035e−03	1.9406	5.1617e−04	1.9070	2.8061e−04	1.9011
$\tau = 0.2$	240	3.9299e−04	1.9357	1.3616e−04	1.9225	7.9134e−05	1.8262
	480	1.0063e−04	1.9655	3.5080e−05	1.9566	2.1035e−05	1.9115
	60	7.1823e−03	–	2.2843e−03	–	1.2069e−03	–
$u_B = 0.75$	120	1.8963e−03	1.9213	6.1315e−04	1.8974	3.4013e−03	1.8272
$\tau = 1$	240	4.8284e−04	1.9736	1.5796e−04	1.9567	9.0912e−04	1.9035
	480	1.2093e−04	1.9974	3.9783e−05	1.9894	2.3121e−05	1.9753
	60	1.1042e−02	–	3.5020e−03	–	1.8299e−03	–
$u_B = 0.75$	120	3.0287e−03	1.8662	9.1181e−04	1.9414	4.8976e−04	1.9016
$\tau = 5$	240	8.0111e−04	1.9186	2.3118e−04	1.9797	1.2593e−04	1.9595
	480	2.1076e−04	1.9264	5.8358e−05	1.9860	3.1627e−05	1.9934

The final time $T = 1$ was employed, so that there was no shock created. ϵ in the MBL Eq. (3.1) is taken to be 1, M is taken to be 2, and the computational interval is $[-10, 20]$. The L_1, L_2, L_∞ order tests of the trapezoid scheme and the third order semi-discrete scheme with different parameter τ values and the initial condition u_B are given in Tables 1 and 2. Table 1 shows that the trapezoid rule achieved second order accuracy for all the tested cases in L_1, L_2, L_∞ sense. Table 2 shows that the semi-discrete scheme has the order of accuracy greater than 2.3 for all the cases, and exceeds 3 for some cases. This confirms the accuracy study given in Sections 2.1.1 and 2.2 respectively.

We will now use examples to study the solutions to MBL Eq. (3.1) using the numerical schemes proposed in Section 2. We first notice that if we scale t and x as follows

$$\tilde{t} = \frac{t}{\epsilon}, \qquad \tilde{x} = \frac{x}{\epsilon},$$

then MBL (3.1) equation can be written in terms of $\tilde{t}$ and $\tilde{x}$ as follows

$$u_{\tilde{t}} + (f(u))_{\tilde{x}} = u_{\tilde{x}\tilde{x}} + \tau u_{\tilde{x}\tilde{x}\tilde{t}}. \tag{3.2}$$

The scaled Eq. (3.2) shows that it is the magnitude of $\frac{t}{\epsilon}$ and $\frac{x}{\epsilon}$ that determine the asymptotic behavior, not t, x, neither ϵ alone [15]. In addition, (3.2) also shows that the dispersive parameter τ denotes the relative importance of the dispersive term u_{xxt}. The bigger τ is, the more dispersive effect Eq. (3.1) has. This can be seen from the computational results to be shown later in this section.

van Duijn et al. [15] numerically provided a bifurcation diagram (Fig. 3) of MBL (3.1) equation as the dispersive parameter τ and the post-shock value u_B of the initial condition vary. The solution of (3.1) has been proven to display qualitatively different profiles for parameter values (τ, u_B) falling in different regimes of the bifurcation diagram. In particular, for every fixed τ value, there are two

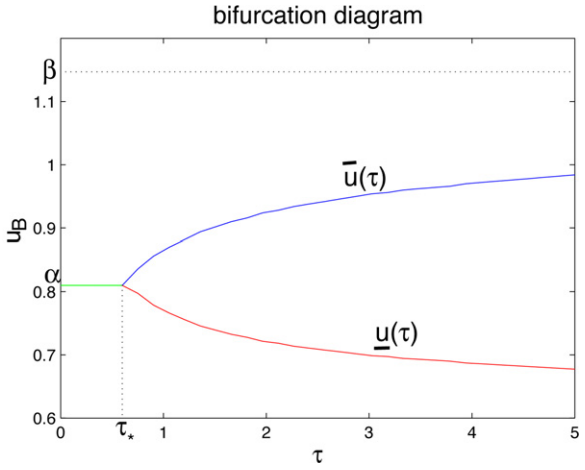

Fig. 3. The bifurcation diagram of the MBL Eq. (1.4) with the bifurcation parameters (τ, u_B).

Table 2
The accuracy test for the third order semi-discrete scheme for the MBL Eq. (3.1) with $\epsilon = 1$ and $M = 2$.

	N	$\left\|\left\| u_{\Delta x} - u_{\frac{\Delta x}{2}} \right\|\right\|_1$	Order	$\left\|\left\| u_{\Delta x} - u_{\frac{\Delta x}{2}} \right\|\right\|_2$	Order	$\left\|\left\| u_{\Delta x} - u_{\frac{\Delta x}{2}} \right\|\right\|_\infty$	Order
	120	2.6992e−03	–	1.1300e−03	–	7.2363e−04	–
$u_B = 0.9$	240	4.0403e−04	2.7400	1.7079e−04	2.7260	1.1283e−04	2.6811
$\tau = 0.2$	480	5.7504e−05	2.8127	2.4624e−05	2.7941	1.6242e−05	2.7963
	960	8.4934e−06	2.7592	3.0892e−06	2.9948	1.7607e−06	3.2055
	120	4.7731e−03	–	2.0192e−03	–	1.7267e−03	–
$u_B = 0.9$	240	8.7205e−04	2.4524	3.6879e−04	2.4529	3.0632e−04	2.4949
$\tau = 1$	480	1.2006e−04	2.8606	5.0480e−05	2.8690	4.1985e−05	2.8671
	960	1.5942e−05	2.9129	6.6663e−06	2.9208	5.1464e−06	3.0282
	120	3.7573e−03	–	1.2122e−03	–	7.9211e−04	–
$u_B = 0.9$	240	7.4624e−04	2.3320	2.4164e−04	2.3267	1.5061e−04	2.3949
$\tau = 5$	480	1.1994e−04	2.6373	3.8434e−05	2.6524	2.5089e−05	2.5857
	960	1.5565e−05	2.9460	4.9190e−06	2.9660	3.1363e−06	2.9999
	120	2.1836e−03	–	9.1039e−04	–	5.7219e−04	–
$u_B = \alpha$	240	3.2729e−04	2.7381	1.3760e−04	2.7260	8.9550e−05	2.6757
$\tau = 0.2$	480	4.6856e−05	2.8043	1.9909e−05	2.7890	1.2935e−05	2.7914
	960	6.7382e−06	2.7978	2.3182e−06	3.1023	1.4109e−06	3.1965
	120	3.9014e−03	–	1.6388e−03	–	1.3873e−03	–
$u_B = \alpha$	240	7.0517e−04	2.4680	2.9669e−04	2.4656	2.4272e−04	2.5149
$\tau = 1$	480	9.6528e−05	2.8690	4.0354e−05	2.8781	3.3125e−05	2.8733
	960	1.2890e−05	2.9047	5.3648e−06	2.9111	4.0754e−06	3.0229
	120	3.0797e−03	–	9.9202e−04	–	6.4456e−04	–
$u_B = \alpha$	240	6.1133e−04	2.3328	1.9783e−04	2.3261	1.2277e−04	2.3924
$\tau = 5$	480	9.7351e−05	2.6507	3.1222e−05	2.6637	2.0263e−05	2.5990
	960	1.2396e−05	2.9733	3.9513e−06	2.9822	2.4962e−06	3.0210
	120	1.8244e−03	–	7.5548e−04	–	4.6671e−04	–
$u_B = 0.75$	240	2.7262e−04	2.7425	1.1419e−04	2.7260	7.3299e−05	2.6707
$\tau = 0.2$	480	3.9198e−05	2.7980	1.6562e−05	2.7855	1.0681e−05	2.7788
	960	5.4739e−06	2.8401	1.9677e−06	3.0733	1.3232e−06	3.0129
	120	3.2727e−03	–	1.3672e−03	–	1.1477e−03	–
$u_B = 0.75$	240	5.8671e−04	2.4798	2.4585e−04	2.4754	1.9866e−04	2.5304
$\tau = 1$	480	7.9974e−05	2.8750	3.3285e−05	2.8848	2.7033e−05	2.8775
	960	1.0724e−05	2.8987	4.4466e−06	2.9041	3.3341e−06	3.0193
	120	2.5902e−03	–	8.3335e−04	–	5.3882e−04	–
$u_B = 0.75$	240	5.1342e−04	2.3348	1.6611e−04	2.3268	1.0271e−04	2.3913
$\tau = 5$	480	8.1062e−05	2.6630	2.6032e−05	2.6738	1.6813e−05	2.6109
	960	1.0173e−05	2.9944	3.2662e−06	2.9946	2.0473e−06	3.0377

critical u_B values, namely, $\bar{u}$ and $\underline{u}$. From the bifurcation diagram (Fig. 3), it is clear that, when $\tau < \tau_*$, $\bar{u} = \underline{u} = \alpha$. For a fixed τ value, the solution has three different profiles.

(a) If $u_B \in [\bar{u}, 1]$, the solution contains a plateau value u_B for $0 \le \frac{x}{t} \le \frac{df}{du}(u_B)$, a rarefaction wave connecting u_B to $\bar{u}$ for $\frac{df}{du}(u_B) \le \frac{x}{t} \le \frac{df}{du}(\bar{u})$, another plateau value $\bar{u}$ for $\frac{df}{du}(\bar{u}) < \frac{x}{t} < \frac{f(\bar{u})}{\bar{u}}$, and a shock from $\bar{u}$ down to 0 at $\frac{x}{t} = \frac{f(\bar{u})}{\bar{u}}$ (see Fig. 4(a)).

(b) If $u_B \in (\underline{u}, \bar{u})$, the solution contains a plateau value u_B for $0 \le \frac{x}{t} < \frac{f(\bar{u})-f(u_B)}{\bar{u}-u_B}$, a shock from u_B up to $\bar{u}$ at $\frac{x}{t} = \frac{f(\bar{u})-f(u_B)}{\bar{u}-u_B}$, another plateau value $\bar{u}$ for $\frac{f(\bar{u})-f(u_B)}{\bar{u}-u_B} < \frac{x}{t} < \frac{f(\bar{u})}{\bar{u}}$, and a shock from $\bar{u}$ down to 0 at $\frac{x}{t} = \frac{f(\bar{u})}{\bar{u}}$ (see Fig. 4(b)). The solution may exhibit a damped oscillation near $u = u_B$.

(c) If $u_B \in (0, \underline{u}]$, the solution consists a single shock connecting u_B and 0 at $\frac{x}{t} = \frac{f(u_B)}{u_B}$ (see Fig. 4(c)). It may exhibit oscillatory behavior near $u = u_B$.

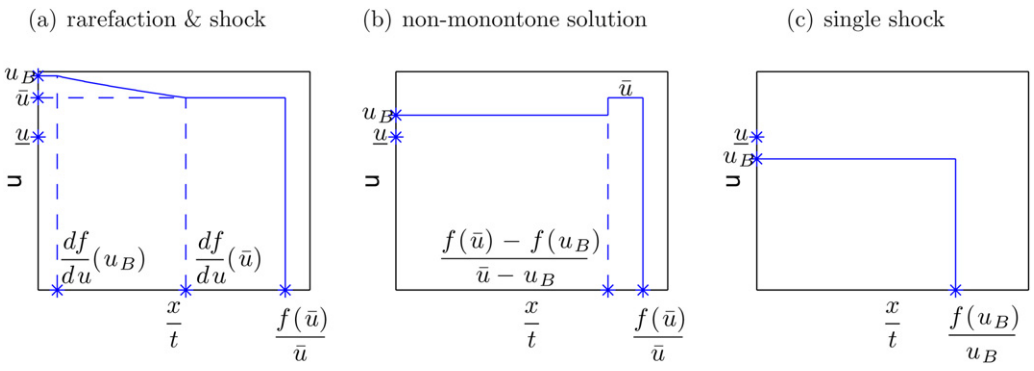

Fig. 4. Given a fixed τ, the three qualitatively different solution profiles due to different values of u_B. In particular, when $\tau > \tau_*$ and $\underline{u} < u_B < \bar{u}$, the solution profile (b) displays non-monotonicity, which is consistent with the experimental observations [4]. (a)–(c) are demonstrative figures.

Table 3
9 pairs of (τ, u_B) values with either fixed τ value or fixed u_B value used in Examples 1–6.

(τ, u_B)	Example 4	Example 5	Example 6
Example 1	(0.2, 0.9)	(1, 0.9)	(5, 0.9)
Example 2	(0.2, α)	(1, α)	(5, α)
Example 3	(0.2, 0.75)	(1, 0.75)	(5, 0.75)

Notice that when $\tau > \tau_*$ and $\underline{u} < u_B < \overline{u}$, the solution profiles (Fig. 4(b)) displays non-monotonicity, which is consistent with the experimental observations [4].

In the numerical computation we show below, we will therefore test the accuracy and capability of central schemes for different parameter values (τ and u_B) that fall into various regimes of the bifurcation diagram, and therefore display qualitatively different solution profiles. The numerical experiments were carried out for $M = 2$, $\epsilon = 0.001$ and $T = 4000 \times \epsilon$, i.e. $\tilde{T} = 4000$ to get the asymptotic solution profiles, and Δx was chosen to be $\frac{\epsilon}{10}$ and $\lambda = \frac{\Delta t}{\Delta x}$ was chosen to be 0.1. The scheme used in the computation is the second order Trapezoid scheme as shown in Section 2.1.1. The Midpoint scheme delivers similar computational results, hence is omitted here. The solution profiles at $\frac{T}{4}$ (blue), $\frac{2*T}{4}$ (green), $\frac{3*T}{4}$ (magenta) and T (black) are chosen to demonstrate the time evolution of the solutions. The red dashed lines are used to denote the theoretical shock locations and plateau values for comparison purpose.

We start with $\tau > 0$. Based on the bifurcation diagram (Fig. 3), we choose three representative u_B values, i.e. $u_B = 0.9 > \alpha$, $u_B = \alpha = \sqrt{\frac{M}{M+1}} = \sqrt{\frac{2}{3}}$ (for $M = 2$) and $u_B = 0.75 < \alpha$. For each fixed u_B, we choose three representative τ values, i.e. $\tau = 0.2 < \tau_* \approx 0.61$, $\tau = 1 > \tau_*$ with $u_B = 0.75 < \underline{u}_{\tau=1} < u_B = \alpha < \overline{u} < u_B = 0.9$, and $\tau = 5$ with $u_B = 0.75, \alpha, 0.9 \in [\underline{u}_{\tau=5}, \overline{u}_{\tau=5}]$. We first use this 9 pairs of (τ, u_B) values given in Table 3 to validate the solution profiles with the demonstrative solution profiles given in Fig. 4.

Example 1. $(\tau, u_B) = (0.2, 0.9), (\tau, u_B) = (1, 0.9), (\tau, u_B) = (5, 0.9)$.

When $u_B = 0.9 > \alpha$ is fixed, we increase τ from 0.2 to 1 to 5 (Fig. 5(a)–(c)), the dispersive effect starts to dominate the solution profile. When $\tau = 0.2$ (Fig. 5(a)), the solution profile is similar to the classical BL equation solution (see Fig. 2(b)), with a rarefaction wave for $\frac{x}{t} \in [f'(u = 0.9), f'(u = \alpha) = f'(u = \overline{u}_{\tau=0.2})]$ and a shock from $u = \alpha$ to $u = 0$ at $\frac{x}{t} = f'(\alpha)$. This corresponds to Fig. 4(a) with $\frac{df}{du}(\overline{u}_{\tau=0.2} = \alpha) = \frac{f(\overline{u}_{\tau=0.2})}{\overline{u}_{\tau=0.2}} = \frac{f(\alpha)}{\alpha}$. When $\tau = 1$ (Fig. 5(b)), the rarefaction wave is between $\frac{x}{t} \in [f'(u = 0.9), f'(u = \overline{u}_{\tau=1})]$ and the solution remains at the plateau value $u = \overline{u}_{\tau=1}$ for $\frac{x}{t} \in \left[f'(u = \overline{u}_{\tau=1}), \frac{f(\overline{u}_{\tau=1})}{\overline{u}_{\tau=1}}\right]$ and the shock occurs at $\frac{x}{t} = \frac{f(\overline{u}_{\tau=1})}{\overline{u}_{\tau=1}}$. This corresponds to Fig. 4(a) with $u_B = 0.9 > \overline{u}_{\tau=1} \approx 0.86$. When $\tau = 5$ (Fig. 5(c)), the solution displays the first shock from $u = 0.9$ to $u = \overline{u}_{\tau=5}$ at $\frac{x}{t} = \frac{f(\overline{u}_{\tau=5}) - f(u_B)}{\overline{u}_{\tau=5} - u_B}$, and then remains at the plateau value $u = \overline{u}_{\tau=5}$ for $\frac{x}{t} \in \left[\frac{f(\overline{u}_{\tau=5}) - f(u_B)}{\overline{u}_{\tau=5} - u_B}, \frac{f(\overline{u}_{\tau=5})}{\overline{u}_{\tau=5}}\right]$ and the second shock occurs at $\frac{x}{t} = \frac{f(\overline{u}_{\tau=5})}{\overline{u}_{\tau=5}}$. This corresponds to Fig. 4(b) with $\underline{u}_{\tau=5} \approx 0.68 < u_B = 0.9 < \overline{u}_{\tau=5} \approx 0.98$. Notice that as τ increases, the rarefaction region shrinks and the plateau region enlarges.

Example 2. $(\tau, u_B) = (0.2, \alpha), (\tau, u_B) = (1, \alpha), (\tau, u_B) = (5, \alpha)$.

When $u_B = \alpha$ is fixed, we increase τ from 0.2 to 1 to 5 (Fig. 5(d)–(f)), the dispersive effect starts to dominate the solution profile. When $\tau = 0.2$, the solution displays one single shock at $\frac{x}{t} = \frac{f(\alpha)}{\alpha}$. For both $\tau = 1$ and $\tau = 5$, the solution has two shocks, one at $\frac{x}{t} = \frac{f(\overline{u}_{\tau=1(\tau=5 \text{ respectively})}) - f(\alpha)}{\overline{u}_{\tau=1(\tau=5 \text{ respectively})} - \alpha}$, and another one at $\frac{x}{t} = \frac{f(\overline{u}_{\tau=1(\tau=5 \text{ respectively})})}{\overline{u}_{\tau=1(\tau=5 \text{ respectively})}}$. For both $\tau = 1$ and $\tau = 5$ (Fig. 5(e) and 5(f)), the solutions correspond to Fig. 4(b), which are consistent with the experimental observations. Notice that as τ increases from 1 to 5, i.e. the dispersive effect increases, the inter-shock interval length increases at every fixed time (compare Fig. 5(e) with Fig. 5(f)). In addition, for a fixed $\tau = 1$ ($\tau = 5$ respectively), as time progresses, the inter-shock interval length increases in the linear fashion (see Fig. 5(e) and (f) respectively)).

Example 3. $(\tau, u_B) = (0.2, 0.75), (\tau, u_B) = (1, 0.75), (\tau, u_B) = (5, 0.75)$.

When $u_B = 0.75 <= \alpha$ is fixed, we increase τ from 0.2 to 1 to 5 (Fig. 5(g)–(i)), the start to dominate the solution profile in the similar fashion as $u_B = 0.9$ and $u_B = \alpha$. Notice that when $\tau = 1$, since $u_B = 0.75$ is very close to $\underline{u}_{\tau=1}$, the solution displays oscillation at $\frac{x}{t} = \frac{f(u_B)}{u_B}$ (Fig. 5(h)). If we increase τ further to $\tau = 5$, the dispersive effect is strong enough to create a plateau value at $\overline{u} \approx 0.98$ (see Fig. 5(i)).

Example 4. $(\tau, u_B) = (0.2, 0.9), (\tau, u_B) = (0.2, \alpha), (\tau, u_B) = (0.2, 0.75)$.

Now, we fix $\tau = 0.2$, decrease u_B from 0.9 to α, to 0.75 (Fig. 5(a), (d) and (g)). If $u_B > \alpha$ the solution consists a rarefaction wave connecting u_B down to α, then a shock from α to 0, otherwise, the solution consists a single shock from u_B down to 0. In all cases, since $\tau = 0.2 < \tau_*$, regardless of the u_B value, the solution will not display non-monotone behavior, due to the lack of dispersive effect.

Example 5. $(\tau, u_B) = (1, 0.9), (\tau, u_B) = (1, \alpha), (\tau, u_B) = (1, 0.75)$.

Now, we fix $\tau = 1$, decrease u_B from 0.9 to α, to 0.75 (Fig. 5(b), (e), and (h)). If $u_B = 0.9 > \overline{u}_{\tau=1}$, the solution consists a rarefaction wave connecting u_B and $\overline{u}$, and a shock connecting $\overline{u}$ down to 0 (Fig. 5(b)). Even if $\underline{u} < u_B < \overline{u}$, because $\tau = 1 > \tau_*$, the solution still has a chance to increase to the plateau value $\overline{u}$ as seen in Fig. 5(e). But, if u_B is too small, for example, $u_B = 0.75 < \underline{u}$, the solution does not increase to $\overline{u}$ any more, instead, it consists a single shock connecting u_B down to 0 (Fig. 5(h)).

Example 6. $(\tau, u_B) = (5, 0.9), (\tau, u_B) = (5, \alpha), (\tau, u_B) = (5, 0.75)$.

Now, we fix $\tau = 5$, decrease u_B from 0.9 to α, to 0.75 (Fig. 5(c), (f) and (i)). For all three u_B, they are between $\underline{u}_{\tau=5}$ and $\overline{u}_{\tau=5}$, hence all increase to the plateau value $\overline{u}_{\tau=5} \approx 0.98$ before dropping to 0. Notice that as u_B decreases, the inter-shock interval length decreases at every fixed time (compare Fig. 5(c), (f) and (i)). This shows that when the dispersive effect is strong ($\tau > \tau_*$), the bigger u_B is, the bigger region the solution stays at the plateau value.

Example 7. $(\tau, u_B) = (0, 0.9), (\tau, u_B) = (0, \alpha), (\tau, u_B) = (0, 0.75)$.

We now show the solution profiles for the extreme τ value, i.e. $\tau = 0$ in Fig. 6(a) ($u_B = 0.9$), (b) ($u_B = \alpha$) and 6(c) ($u_B = 0.75$). Notice that these are cases of classical BL equation with small diffusion ϵu_{xx}. We compare Fig. 6(a)–(c) with the solution of the classical BL equation given in Fig. 2(a) and (b), it is clear that they show qualitatively same solution profiles. The difference is that due to the diffusion term in the MBL equation, as shown in Fig. 6, the solutions do not have sharp edges right at the shock, instead, the solutions smear out a little. Notice that this smearing effect is also partially introduced by the central scheme. It is well known that central scheme is non-oscillatory, i.e. it generates numerical viscosity. If we compare Fig. 6(a)–(c) with Fig. 5(a), (d) and (g), there is no visible difference. This shows that once $\tau < \tau_*$, solution profile will stay the same for a fixed u_B value.

Example 8. $(\tau, u_B) = (5, 0.99), (\tau, u_B) = (5, 0.98), (\tau, u_B) = (5, 0.97)$.

We also study the solution profiles for u_B close to $\overline{u}$. For example, when $\tau = 5$, $\overline{u} \approx 0.98$, we hence choose $u_B = 0.99$, $u_B = 0.98$, $u_B = 0.97$ and solutions are shown in Fig. 7(a)–(c). If $u_B = 0.99 > \overline{u}_{\tau=5} \approx 0.98$, the solution drops to the plateau value $\overline{u}$, then drops to 0 (see Fig. 7(a)). If $u_B = 0.98 \approx \overline{u}_{\tau=5}$, the solution remains at plateau value $\overline{u}_{\tau=5}$ and then drop to 0 (see Fig. 7(b)). If $u_B = 0.97 < \overline{u}_{\tau=5}$, the solution increases to the plateau value $\overline{u}_{\tau=5} \approx 0.98$, then drops to 0 (see Fig. 7(c)). In all cases, the transition from u_B to $\overline{u}_{\tau=5} \approx 0.98$ takes very small space. In the majority space, the solution keeps to be the plateau value $\overline{u}_{\tau=5} \approx 0.98$.

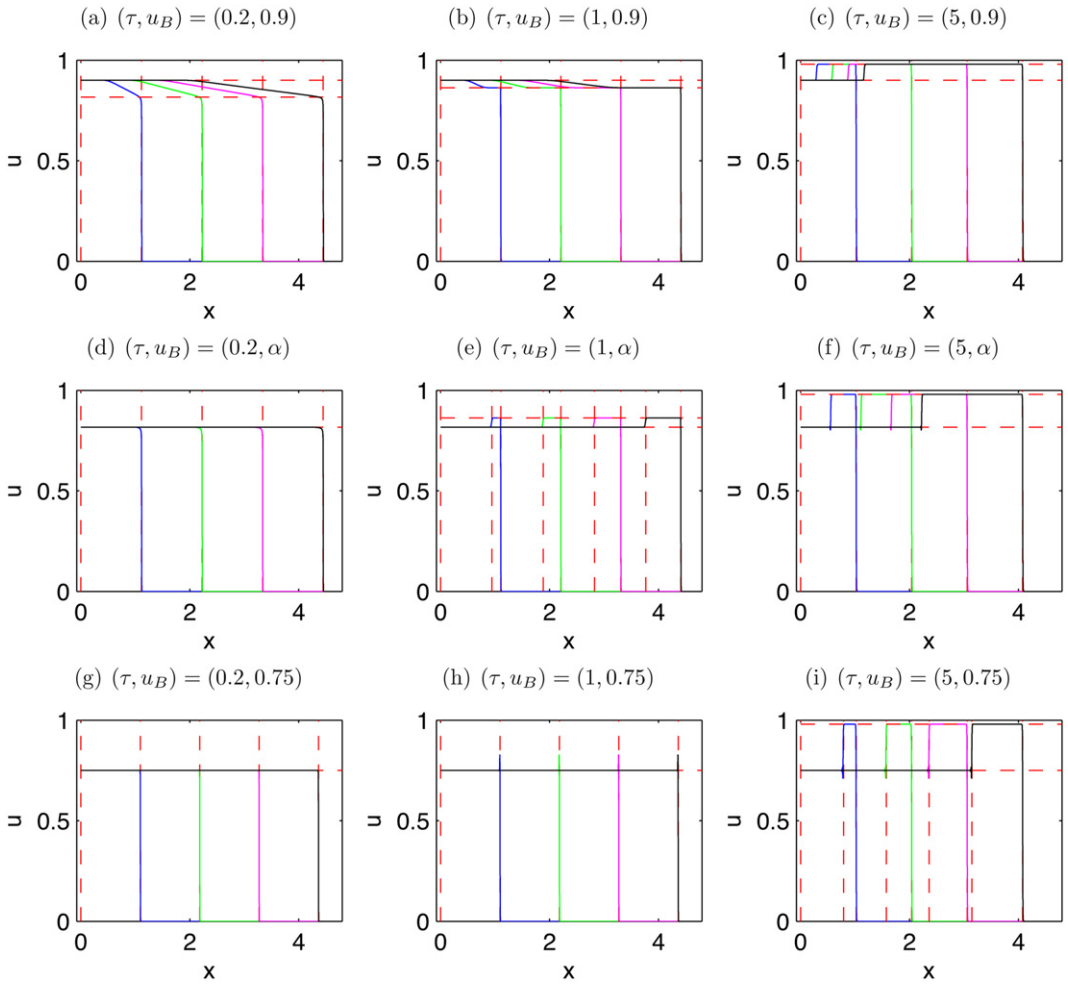

Fig. 5. Numerical solutions to MBL equation with parameter settings fall in different regimes of the bifurcation diagram (Fig. 3). The color coding is for different time: $\frac{1}{4}T$ (blue), $\frac{2}{4}T$ (green), $\frac{3}{4}T$ (magenta) and T (black). The results are discussed in examples 1–6. In figures (d)–(f), $\alpha = \sqrt{\frac{M}{M+1}} = \sqrt{\frac{2}{3}}$ for $M = 2$. (For interpretation of the references to color in this figure legend, the reader is referred to the web version of this article.)

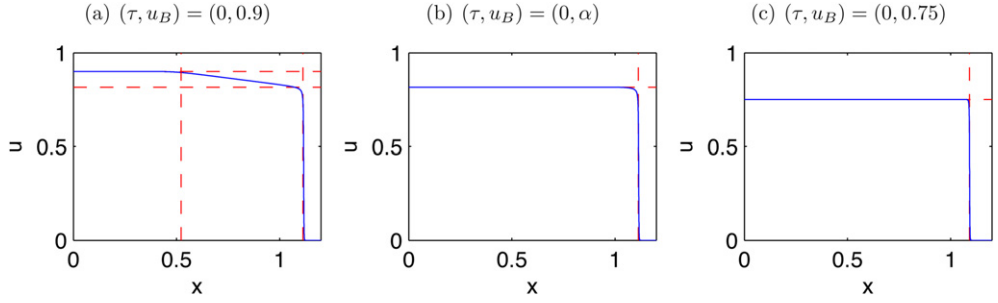

Fig. 6. The numerical solutions of the MBL equation at $T = 1$ with $\tau = 0$ and different u_B values. The results are discussed in example 7.

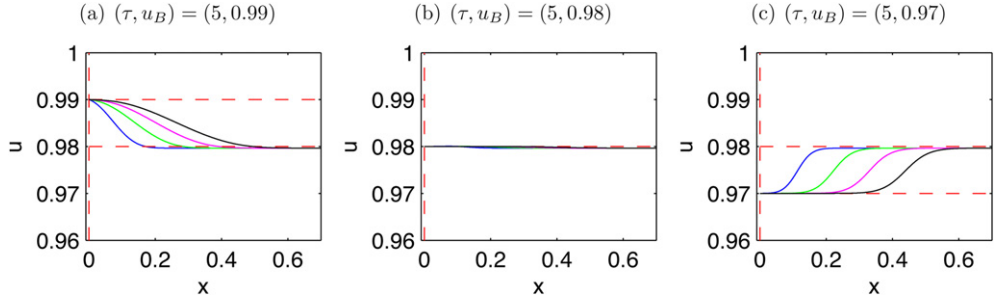

Fig. 7. Numerical solutions to MBL equation with u_B close to $\overline{u}_{\tau=5} \approx 0.98$. The color coding is for different time: $\frac{1}{4}T$ (blue), $\frac{2}{4}T$ (green), $\frac{3}{4}T$ (magenta) and T (black). The results are discussed in example 8. (For interpretation of the references to color in this figure legend, the reader is referred to the web version of this article.)

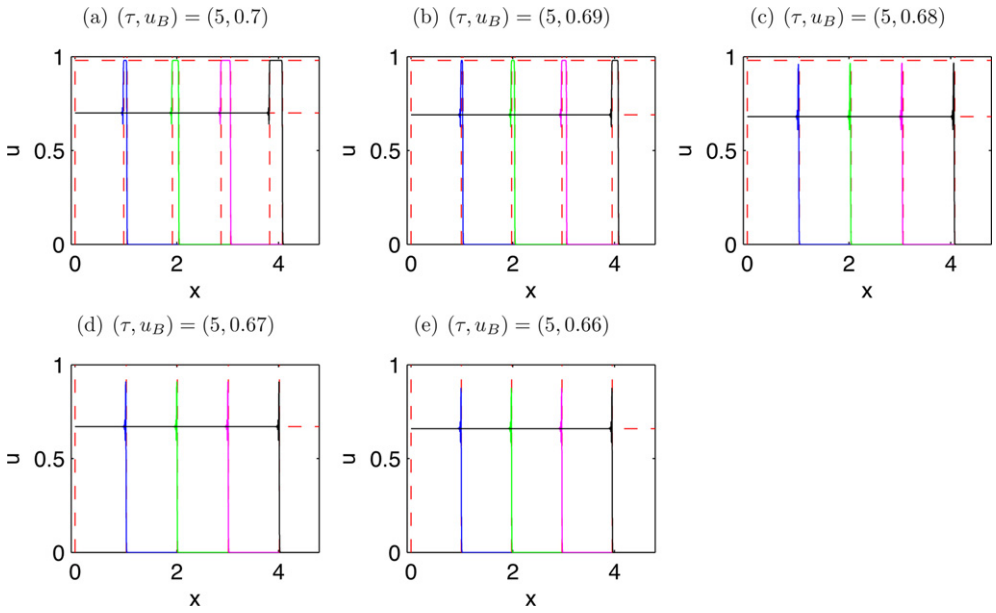

Fig. 8. Numerical solutions to MBL equation with u_B close to $\overline{u}_{\tau=5} \approx 0.68$. The color coding is for different time: $\frac{1}{4}T$ (blue), $\frac{2}{4}T$ (green), $\frac{3}{4}T$ (magenta) and T (black). The results are discussed in example 9. (For interpretation of the references to color in this figure legend, the reader is referred to the web version of this article.)

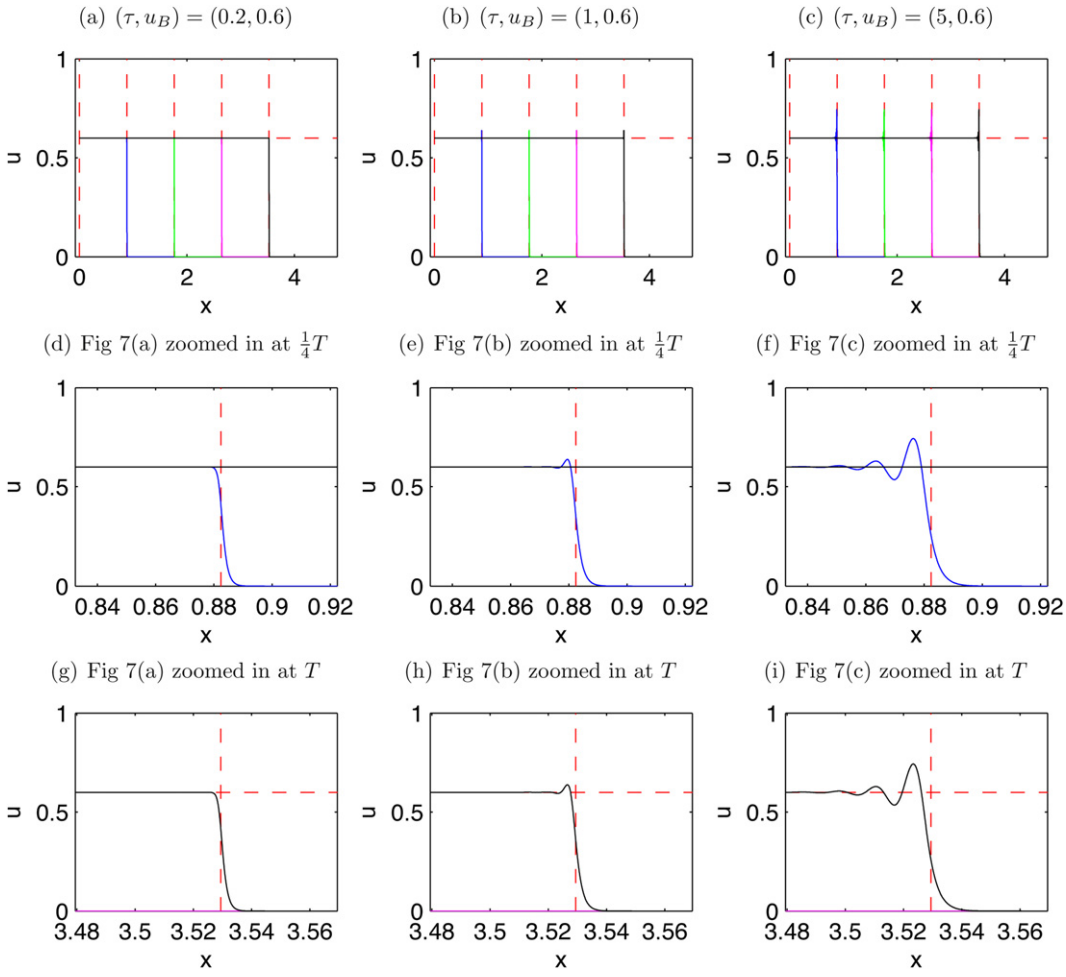

Fig. 9. Numerical solutions to MBL equation with small constant $u_B = 0.6$ and different τ values. The figures on the second and third rows are the magnified versions of the first row at $t = \frac{1}{4}T$ and $t = T$ respectively. The color coding is for different time: $\frac{1}{4}T$ (blue), $\frac{2}{4}T$ (green), $\frac{3}{4}T$ (magenta) and T (black). The results are discussed in examples 10. (For interpretation of the references to color in this figure legend, the reader is referred to the web version of this article.)

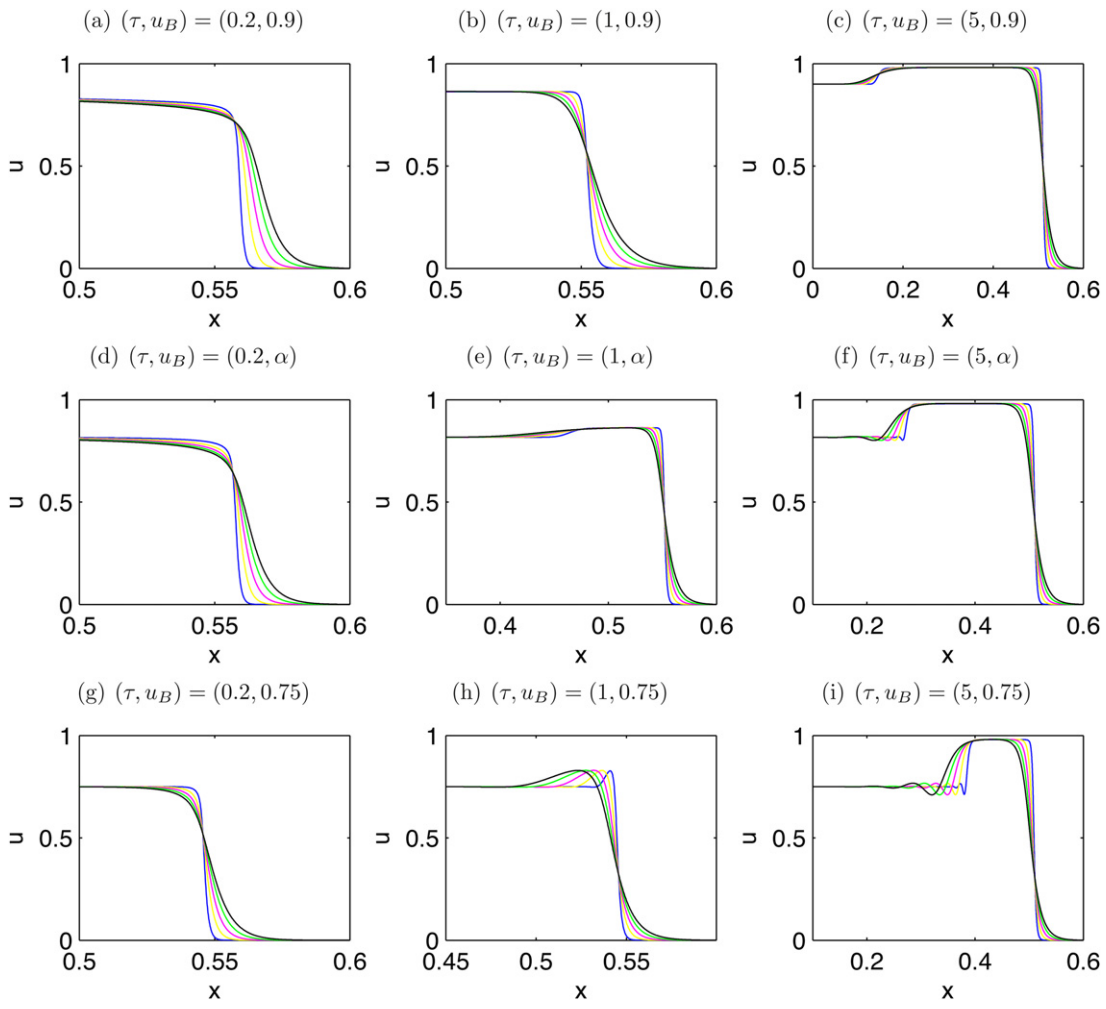

Fig. 10. The numerical solutions of MBL equation at $T = 0.5$ with $\epsilon = 0.001$ (blue), $\epsilon = 0.002$ (yellow), $\epsilon = 0.003$ (magenta), $\epsilon = 0.004$ (green), and $\epsilon = 0.005$ (black). The view windows are zoomed into the regions where different ϵ values impose different solution profiles. The results are discussed in example 11. (For interpretation of the references to color in this figure legend, the reader is referred to the web version of this article.)

Example 9. $(\tau, u_B) = (5, 0.7), (\tau, u_B) = (5, 0.69), (\tau, u_B) = (5, 0.68), (\tau, u_B) = (5, 0.67), (\tau, u_B) = (5, 0.66)$.

In addition, we study the solution profiles for u_B close to $\underline{u}$. For example, when $\tau = 5$, $\underline{u} \approx 0.68$, we hence choose $u_B = 0.7$, $u_B = 0.69$, $u_B = 0.68$, $u_B = 0.67$, $u_B = 0.66$ and solutions are shown in Fig. 8(a)–(e). As u_B decreases crossing $\underline{u}_{\tau=5} \approx 0.68$, the solution gradually stops increasing to the plateau value $\overline{u}_{\tau=5}$, and the inter-shock interval length decreases (compare Fig. 8(a)–(c)). The oscillation in Fig. 8(d) and (e) are due to the fact that u_B values are too close to $\underline{u}_{\tau=5}$. This confirms that even with big dispersive effect (say $\tau = 5$), if u_B is too small (e.g. $u_B < \underline{u}$), the solution will not exhibit non-monotone behavior.

Example 10. $(\tau, u_B) = (0.2, 0.6), (\tau, u_B) = (1, 0.6), (\tau, u_B) = (5, 0.6)$.

We fix u_B to be small, and in this example, we take it to be $u_B = 0.6$. We vary the τ value, from $\tau = 0.2 < \tau_*$ to $\tau = 1$ barely larger than τ_* to $\tau = 5 > \tau_*$. The numerical solutions are given in Fig. 9(a)–(c). As τ increases, the post-shock value remains the same, but there will be oscillation generated as τ becomes larger than τ_*. Fig. 9(d)–(f) show that as τ increases, the oscillation amplitude increases and oscillates more rounds. Notice that τ is the dispersive parameter, and this means that even for small u_B value, different dispersive parameter values still give different dispersive effects, although none can bring the solution to the plateau value $\overline{u}$. Comparing Fig. 9(d)–(f) with Fig. 9(g)–(i), it is clear that the oscillation amplitude remains steady with respect to time.

Example 11. $\epsilon = 0.001, \epsilon = 0.002, \epsilon = 0.003, \epsilon = 0.004, \epsilon = 0.005$.

In this example, we will compare the solution profiles for different ϵ values. Fixing $T = 0.5$, $\Delta x = 0.0001$, $\lambda = \frac{\Delta t}{\Delta x} = 0.1$, we show the numerical results in Fig. 10 for $\epsilon = 0.001$ (blue), $\epsilon = 0.002$ (yellow), $\epsilon = 0.003$ (magenta), $\epsilon = 0.004$ (green), and $\epsilon = 0.005$ (black). For the purpose of cross reference, we choose the same nine sets of parameter settings as in examples 1–6. To assist the observation, the figures in Fig. 10 are zoomed into the regions where different ϵ values introduce different solution profiles. The numerical solutions clearly show that as ϵ increases, the numerical solution is smeared out, and the jump location becomes less accurate. Notice that τ is responsible for the competition between the diffusion and dispersion, which in turn determines the plateau values. Hence varying ϵ value does not affect the plateau location.

4. Conclusion

We extended the second and third order classical central schemes originally designed for the hyperbolic systems to solve the MBL equation, which is of pseudo-parabolic type. The numerical solutions for qualitatively different parameter values τ and initial conditions u_B show that the jump locations are consistent with the theoretical calculation and the plateau heights are consistent with the numerically obtained values given in [15]. In particular, when $\tau > \tau_*$, for $u_B \in (\underline{u}, \overline{u})$, the numerical solutions give non-monotone

water saturation profiles, which is consistent with the experimental observations. In addition, the order tests show that the proposed second and third order central schemes achieved the desired accuracies.

In [16,14], the two-dimensional space extension of the modified Buckley–Leverett equation has been derived. One of the future directions is to develop high order numerical schemes to solve the two-dimensional MBL equation. Central schemes have been used to solve high dimensional hyperbolic problem and dispersive problem [7,12], which makes it a good candidate for such a task.

Acknowledgments

CYK would like to thank Prof. L.A. Peletier for introducing MBL equation.

References

[1] S. Buckley, M. Leverett, Mechanism of fluid displacement in sands, Petrol. Trans. AIME 146 (1942) 107–116.
[2] B. Cockburn, C. Johnson, C.-W. Shu, E. Tadmor, Advanced numerical approximation of nonlinear hyperbolic equations, in: Alfio Quarteroni, Fondazione C.I.M.E. [C.I.M.E. Foundation] (Eds.), Vol. 1697 of Lecture Notes in Mathematics, Springer-Verlag, Berlin (Papers From the C.I.M.E. Summer School Held in Cetraro, June 23–28, 1997), 1998.
[3] B. Cockburn, G.E. Karniadakis, C.-W.E. Shu, Discontinuous Galerkin methods: theory, computation and applications, Lect. Notes Comput. Sci. Eng. (2000).
[4] D.A. DiCarlo, Experimental measurements of saturation overshoot on infiltration, Water Resour. Res. 40 (April) (2004), 4215.1–4215.9.
[5] S. Hassanizadeh, W. Gray, Mechanics and thermodynamics of multiphase flow in porous media including interphase boundaries, Adv. Water Resour. 13 (1990) 169–186.
[6] S. Hassanizadeh, W. Gray, Thermodynamic basis of capillary pressure in porous media, Water Resour. Res. 29 (1993) 3389–3405.
[7] G.-S. Jiang, E. Tadmor, Nonoscillatory central schemes for multidimensional hyperbolic conservation laws, SIAM J. Sci. Comput. 19 (6) (1998) 1892–1917 (electronic), URL: http://dx.doi.org/10.1137/S106482759631041X.
[8] A. Kurganov, D. Levy, A third-order semidiscrete central scheme for conservation laws and convection-diffusion equations, SIAM J. Sci. Comput. 22 (4) (2000) 1461–1488 (electronic), URL: http://dx.doi.org/10.1137/S1064827599360236.
[9] A. Kurganov, C.-T. Lin, On the reduction of numerical dissipation in central-upwind schemes, Commun. Comput. Phys. 2 (1) (2007) 141–163.
[10] R.J. LeVeque, Numerical methods for conservation laws, in: Lectures in Mathematics ETH Zürich, 2nd ed., Birkhäuser Verlag, Basel, 1992.
[11] R.J. LeVeque, Finite volume methods for hyperbolic problems, in: Cambridge Texts in Applied Mathematics, Cambridge University Press, Cambridge, 2002.
[12] D. Levy, G. Puppo, G. Russo, Compact central WENO schemes for multidimensional conservation laws, SIAM J. Sci. Comput. 22 (2) (2000) 656–672, URL: http://dx.doi.org/10.1137/S1064827599359461.
[13] H. Nessyahu, E. Tadmor, Nonoscillatory central differencing for hyperbolic conservation laws, J. Comput. Phys. 87 (2) (1990) 408–463.
[14] C.J. van Duijn, A. Mikelic, I. Pop, Effective Buckley–Leverett equations by homogenization, in: Progress in Industrial Mathematics at ECMI, 2000, pp. 42–52.
[15] C.J. van Duijn, L.A. Peletier, I.S. Pop, A new class of entropy solutions of the Buckley–Leverett equation, SIAM J. Math. Anal. 39 (2) (2007) 507–536 (electronic), URL: http://www.dx.doi.org/10.1137/05064518X.
[16] Y. Wang, Central schemes for the modified Buckley–Leverett equation, Ph.D. thesis, The Ohio State University, 2010.
[17] Y. Wang, C.-Y. Kao, Bounded domain problem for the modified Buckley–Leverett equation, submitted for publication.
[18] Y. Xu, C.-W. Shu, A local discontinuous Galerkin method for the Camassa–Holm equation, SIAM J. Numer. Anal. 46 (4) (2008) 1998–2021, URL: http://dx.doi.org/10.1137/070679764.
[19] Y. Xu, C.-W. Shu, Local discontinuous Galerkin method for the Hunter–Saxton equation and its zero-viscosity and zero-dispersion limits, SIAM J. Sci. Comput. 31(2) (2008/09) 1249–1268, URL: http://dx.doi.org/10.1137/080714105.

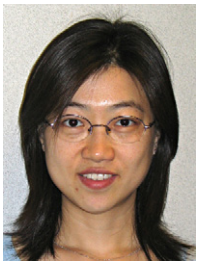

Ying Wang completed her PhD in Mathematics at the Ohio State University. She is currently a Dunham Jackson assistant professor at school of Mathematics, university of Minnesota. Her research interests include Mathematical modeling, scientific computing, image processing, Mathematical biology.

Chiu-Yen Kao completed her PhD in Mathematics at University of California, Los Angeles. She is currently an associate professor at the Ohio State University and a visiting associate professor at Claremont Mckenna College. Her research interests include shape optimization problem for elliptic eigenvalue problems, Mathematical biology, numerical methods for hyperbolic equations and dispersive equations.